Progress in the Development of Global Medium-Energy Nucleon-Nucleus Optical Model Potentials

D. G. Madland

Theoretical Division, Los Alamos National Laboratory
Los Alamos, New Mexico 87545

Abstract

Two existing global medium-energy nucleon-nucleus phenomenological optical model potentials are described and compared with experiment and with each other. The first of these employs a Dirac approach (second-order reduction) that is global in projectile energy and projectile isospin and applies to the target nucleus ^{208}Pb. Here the standard S-V (isoscalar-scalar, isoscalar-vector) model has been extended to include the corresponding isovector components by introduction of a relativistic Lane model. The determination of the energy range, energy dependence, and isospin dependence are discussed, as are the predictions for neutron scattering observables, and also the correlations and ambiguities found in Dirac phenomenology. The second of these employs a relativistic equivalent to the Schrödinger equation (including relativistic kinematics) that is global in projectile energy, projectile isospin, and target (Z,A). Here, particular attention is given to predictions for the integrated scattering observables – neutron total cross sections and proton total reaction cross sections – and their sensitivity to the absorptive parts of the potential. Finally, current work is described and the influence of the nuclear bound state problem (treated in relativistic mean field theory) on the Dirac scattering problem is mentioned. Spherical target nuclei are treated in the present work and strongly-collective target nuclei (rotational and vibrational) requiring coupled-channels approaches will be treated in a future paper.

A Global Phenomenological Dirac Potential

The potential described in this section consists of a global medium-energy nucleon-nucleus phenomenological Dirac potential for the target nucleus ^{208}Pb. The potential is global in projectile energy and projectile isospin and it was determined [1] by least-squares adjustment of calculated scattering observables (model parameters) with respect to corresponding measured scattering observables for both proton and neutron scattering over a wide range in projectile energy.

The Dirac equation is used in the mean field approximation by which the nucleon (meson) fields are replaced by their expectation values. Proton-nucleus (or neutron-nucleus) scattering is then described using isoscalar-scalar and isoscalar-vector mean fields. Here these are taken, respectively, as a spherically symmetric complex Lorentz scalar potential $S_0(r, E, ...)$ corresponding to the (fictitious) σ meson field and a spherically symmetric complex Lorentz vector potential $V_0(r, E, ...)$ (time-like component of Lorentz four-vector) corresponding to the ω meson field, together with a spherically symmetric Coulomb potential V_c.

However, a description of *nucleon-nucleus* scattering requires the explicit addition of isovector-scalar and isovector-vector potentials (mean fields) $S_1(r, E, ...)$ and $V_1(r, E, ...)$, respectively, yielding

$$S = S_0 \pm \epsilon\, S_1 \tag{1}$$

$$V = V_0 \pm \epsilon\, V_1 \tag{2}$$

$$\epsilon = 4\,\vec{T}\cdot\vec{\tau}/A = (N-Z)/A\ . \tag{3}$$

In these equations S_1 and V_1 correspond to δ meson and ρ meson mean fields, respectively, and we use the nuclear physics isospin convention: $\tau_3(neutron) = +\frac{1}{2}$, $\tau_3(proton) = -\frac{1}{2}$. Equations (1)–(3) are a relativistic generalization of the Lane model [2].

With this scalar-vector interaction including isospin the Dirac equation becomes ($\hbar = c = 1$)

$$[\vec{\alpha}\cdot\vec{p} + \beta\{m + S\}]\psi = [E - V - V_c]\psi \tag{4}$$

where ψ is a four-component Dirac spinor with upper and lower components ψ_U and ψ_L , E is the total energy of the scattered nucleon in the c.m. frame, $\vec{\alpha}$ and β are four Hermitian operators acting on the spin variables alone (these are related to the Dirac γ matrices), and ψ contains a two-component isospinor which is an eigenvector of τ_3 appearing in S and V. A second-order reduction for the upper component ψ_U yields

$$[p^2 + U_c + U_{so}\{(\vec{\sigma} \cdot \vec{L}) - i(\vec{r} \cdot \vec{p})\}]\psi_U = [(E - V_c)^2 - m^2]\psi_U \tag{5}$$

where the effective central potential U_c is given by

$$U_c = [2\,E\,V + 2\,m\,S - V^2 + S^2 + U_{cc}]/2\,E \tag{6}$$

the Coulomb correction term U_{cc} (numerator) is

$$U_{cc} = -2\,V_c\,V \tag{7}$$

and the spin-orbit term U_{so} is

$$U_{so} = -\frac{1}{2E}\left\{\frac{1}{r}\,\frac{1}{E + m + S - V - V_c}\,\frac{\partial}{\partial r}(S - V - V_c)\right\} . \tag{8}$$

It is worth noting that S and V appear both linearly and quadratically in the effective central potential U_c leading *naturally* to the "wine-bottle"shapes required to describe medium-energy nucleon-nucleus scattering somewhat below the transition region (where the sign of U_c changes) [3]. Also, the Coulomb correction and spin-orbit terms both appear *naturally* in the Dirac formalism whereas they are *ad hoc* in the Schrödinger formalism.

Equation (5) is solved for the extensive ^{208}Pb data set by making the following assumptions (due to *tractability* and the fact that there exists much more proton data than neutron data): (1) the geometries of the potentials are independent of projectile species and projectile energy, so that all energy dependence and isospin dependence is contained in the strengths of the potentials, and (2) the same geometry exists for the isoscalar and isovector components of a given potential. With these assumptions

$$U = U_0(T, \epsilon)\,g(r) \tag{9}$$

where U_0 is a strength, T is the projectile kinetic energy in the laboratory system, and $g(r)$ is a geometric form factor taken to be a symmetrized Woods-Saxon shape (which has a closed-form Fourier transform) given by

$$g(r) = [1 + exp\left(\frac{r - c}{a}\right)]^{-1}\,[1 + exp\left(-\frac{r + c}{a}\right)]^{-1} \tag{10}$$

where c and a are the radius and diffuseness parameters, respectively, and c is assumed to be of the usual form $c = r_0\,A^{\frac{1}{3}}$ with r_0 constant and A the target mass number.

Energy dependence was studied by considering p + ^{208}Pb scattering data *only* which implies that $U_0(T, \epsilon) = U_0(T)$, and six forms of $U_0(T)$ were tested :

$$\begin{aligned} U_0(T) &= U_0 && (11)\\ &= U_0 + \alpha\,T && (12)\\ &= U_0 + \alpha\,ln(T) && (13)\\ &= U_0\,exp(-T/\alpha) && (14)\\ &= U_0\,[1 + (T/\alpha)^2]^{-1} && (15)\\ &= U_0\,[1 + (T/\alpha)^2]^{-\frac{1}{2}} && (16) \end{aligned}$$

The measured proton scattering observables used in studying the energy dependence consist of differential elastic scattering cross sections $d\sigma/d\Omega$, analyzing powers $A_y(\theta)$, spin-rotation functions $Q(\theta)$, and total

reaction cross sections σ_R, all as a function of laboratory proton energy T_p for the ^{208}Pb target. Considering experimental data over the range 80 to 800 MeV the minimum values of chi-square/point/energy (data set) are shown in Fig. 1 for four of the six energy dependencies chosen for study [the other two, Eqs. (15) and (16), yielded poorer results, on average, than the linear, log, or exponential energy dependencies]. The figure shows that no energy dependence is inadmissable and that none of the three energy dependencies shown is admissable over the entire energy range shown. The results of reducing the proton energy range are shown in Fig. 2 for these three energy dependencies. Clearly, a factor ~ 5 improvement in the total chi-square/point is obtained by reducing the proton energy range from 80–800 MeV to 95–300 MeV. Note, however, that the total chi-square/point is almost equivalent for the energy range of 95–500 MeV. The remainder of this section addresses the smallest of these three energy ranges: 95–300 MeV.

The isospin dependence was studied by including the n + ^{208}Pb scattering data (consisting of neutron total cross sections σ_T as a function of laboratory neutron energy T_n) with the proton data, for the energy range 95–300 MeV. Two energy dependencies were chosen to study the isospin dependence. These are the logarithmic energy dependence, Eq. (13), which yields the best chi-square/point of all cases studied and has an energy-independent isospin dependence by construction (as does the linear assumption which has a slightly worse chi-square/point) and the exponential energy dependence, Eq. (14), which has an energy dependent isospin dependence by construction. Thus, the two potential strengths tested are of the form

$$U_0(T,\epsilon) = B \pm \epsilon\, C + \alpha\, ln(T) \quad (17)$$

$$= [B \pm \epsilon\, C]\; exp(-T/\alpha) \quad (18)$$

where B, C, and α are the constants to be determined for each of the four terms of the complete complex scalar-vector interaction potential. The chi-square minimization led to a logarithmic model that gives slightly better fits to the neutron data ($\chi^2_{tot}(n)$/point of 0.90 *vs* 0.95) and the proton data ($\chi^2_{tot}(p)$/point of 12 *vs* 13) than the exponential model and a total-chi square, χ^2_{tot}/point, for combined neutron and proton data, of 12.0 for the logarithmic model *vs* 12.8 for the exponential model. The best-fit potentials for these two choices of the energy and isospin dependence, Eqs. (17) and (18), are given in Table I.

Table I. Best-fit Dirac global optical potentials for nucleon plus ^{208}Pb scattering in the energy interval $95 \leq T \leq 300$ MeV.[1]

	Logarithmic Model	**Exponential Model**
Scalar Real	$SR = -570 \mp 307\epsilon + 23.1 ln(T)$	$SR = (-491 \mp 362\epsilon) exp(-T/5440)$
	$r_0 = 1.105$ $\quad a = 0.692$	$r_0 = 1.102$ $\quad a = 0.700$
Scalar Imag.	$SI = 237 \mp 71.1\epsilon - 42.0 ln(T)$	$SI = (52.6 \mp 125\epsilon) exp(-T/164.2)$
	$r_0 = 1.157$ $\quad a = 0.512$	$r_0 = 1.153$ $\quad a = 0.488$
Vector Real	$VR = 532 \pm 235\epsilon - 37.4 ln(T)$	$VR = (399 \pm 287\epsilon) exp(-T/1686)$
	$r_0 = 1.109$ $\quad a = 0.664$	$r_0 = 1.105$ $\quad a = 0.676$
Vector Imag.	$VI = -189 \pm 54.2\epsilon + 28.9 ln(T)$	$VI = (-54.8 \pm 60.4\epsilon) exp(-T/512.2)$
	$r_0 = 1.149$ $\quad a = 0.633$	$r_0 = 1.137$ $\quad a = 0.647$

Figures 3 and 4 show fits to p + ^{208}Pb data at 200 MeV using the proton-only potentials and the neutron-plus-proton potentials (Table I) for both the logarithmic and exponential models. As can be seen, the fits are quite good for both models for both input data sets. In fact, on the basis of this 200 MeV proton data, one cannot determine the preferred model and there appears to be only a slight preference for the neutron-plus-proton input data over the proton-only input data. However, the fits to the n + ^{208}Pb total cross section data for the identical two models and identical two input data sets, Fig. 5, show only qualitative agreement in the case of the proton-only input data whereas quite good agreement is obtained in the case of the neutron-plus-proton input data. In addition, the data indicate a slight preference for the logarithmic model over the exponential model. Furthermore, the predictive power of the identical two models and identical two input data sets is tested against n + ^{208}Pb differential elastic cross section and analyzing power data at 155

[1] Strengths are in MeV and geometry is in fm; the upper (lower) signs refer to neutrons (protons).

MeV [4] that were not included in the input data. Figure 6 shows that both potentials give similarly good predictions, but that the analyzing power data clearly prefers the neutron-plus-proton input data. Thus, Figs. 3–6 lead to the conclusions that a medium-energy phenomenological *nucleon-nucleus* potential may be the best way to proceed and (somewhat weaker) that an isoscalar logarithmic energy dependence and an isovector energy independence may be more physical than an exponential energy dependence for both isoscalar and isovector components.

Given these conclusions the logarithmic model (Table I) was used to predict unmeasured neutron elastic scattering angular distributions, analyzing powers, and spin-rotation functions at 100, 200, and 300 MeV [5]. These are shown in Fig. 7 for 100 MeV as are the corresponding predictions for proton scattering also using the logarithmic model. The differences between the three observables for neutron and proton scattering, at 200 and 300 MeV as well as 100 MeV, were studied by also performing calculations for a "gedanken" projectile with potential strengths appropriate to a proton, but with the charge set to zero. The study concluded that (a) the shift in the first minimum of the differential cross sections is due to the influence of the Coulomb interaction, while the enhanced magnitude of the back-angle neutron cross sections results from the difference in sign of the isovector strengths, (b) the saturation of the neutron analyzing powers (+1.0) appears to come solely from the absence of the Coulomb interaction, and (c) the damping of the large-angle oscillations of the neutron spin-rotation functions largely arises from the difference in sign of the isovector strengths, although the absence of the Coulomb interaction plays some role.

Finally, the correlations and ambiguities found in Dirac phenomenology were studied [6] for a single case, that of p + ^{40}Ca at 181 MeV. Briefly, two equivalent families of potentials are found, only one of which predicts the correct total reaction cross section (the measured value was *not* used in determining the best-fit parameterization), and has a just slightly lower χ^2 than that of the minimum in the other family. As one might expect, relatively large ambiguities are found in the imaginary strengths and they are linearly correlated. Also, the real geometries are particularly stable and the real strengths are also correlated, but are much better determined than the imaginary strengths. The point to understand is that the observed total reaction cross section is able to distinguish the correct Dirac phenomenological potential family.

A Global Phenomenological Schrödinger Potential

The potential described in this section consists of a global medium-energy nucleon-nucleus phenomenological relativistic Schrödinger potential. The potential is global in projectile energy, projectile isospin, and target (Z,A). It employs relativistic kinematics and a relativistic equivalent to the Schrödinger equation obtained by appropriate reduction of the Dirac equation for a massive energetic fermion (m, k) moving in a localized central potential $V(r)$ taken as the time-like component of a Lorentz four-vector. The resultant radial equation for the partial wave $f_L(\rho)$ is given by ($\hbar = c = 1$)

$$\left\{ \frac{d^2}{d\rho^2} + \left[1 - \frac{U(\rho)}{T_c} - \frac{L(L+1)}{\rho^2} \right] \right\} f_L(\rho) = 0 \tag{19}$$

where $\rho = kr$, T_c is the total c.m. kinetic energy, L is the orbital angular momentum, and $U(\rho)$ is the renormalized total (nuclear plus Coulomb) optical potential

$$U(\rho) = \gamma\, V(r)\ ,\ \gamma = 1 + \frac{T_c}{T_c + 2m}\ . \tag{20}$$

Equation (19) is formally identical to the radial equation for the solution of the non-relativistic Schrödinger equation for the analogous scattering problem. By way of example, Fig. 8 shows calculations of the proton total reaction cross section for p + ^{27}Al using Eq. (19) in three different ways for the identical potential $V(r)$: (1) non-relativistic (classical kinematics and $\gamma \equiv 1$), (2) relativistic kinematics (and $\gamma \equiv 1$), and (3) relativistic equivalent Schrödinger (relativistic kinematics and $\gamma > 1$). Clearly, the γ factor becomes increasingly important as the projectile kinetic energy increases [Eq. (20)]. Option (3) is used in the remainder of this section.

The starting point for determining this potential was the phenomenological proton optical-model potential of Schwandt *et al.* [7] based upon differential elastic scattering cross sections and analyzing powers for the

mass range $24 \leq A \leq 208$ and proton laboratory kinetic energy range $80 \leq T_p \leq 180$ MeV. The potential employs standard Woods-Saxon form factors. The goals were to extend the mass range of the potential to $12 \leq A \leq 208$, to extend the energy range of the potential to $50 \leq T_p \leq 400$ MeV, and to transform the extended proton potential to a neutron potential for the same mass and energy ranges. Moreover, optimal reproduction of the measured integrated scattering observables, the proton total reaction cross section σ_R and the neutron total cross section σ_T, was the main focus of the work.

The approach used was to (a) adjust *only* the parameters of the proton central absorptive potential to optimally reproduce the measured total reaction cross sections, (b) perform these adjustments allowing only *small* changes in the calculated $d\sigma/d\Omega$ and $A_y(\theta)$, and (c) transform the extended proton potential to the corresponding neutron potential by use of the Lane model [2] and accounting for the Coulomb correction. [Since the proton starting potential [7] does not explicitly contain a Coulomb correction term it is assumed that the term is implicitly present and, therefore, that it must be *subtracted* from the corresponding *neutron* potential. The correction is taken as $0.4\,Z/A^{\frac{1}{3}}$.] The work was performed by iterative computation, that is, a generalized nonlinear least-squares adjustment algorithm was *not* used,[2] for three nuclei spanning a large mass range: ^{27}Al, ^{56}Fe, and ^{208}Pb. The resultant potential gave reasonably satisfactory predictions for both proton and neutron scattering observables for other target A values in the same range [8]. Further iterative computations were performed for six additional nuclei: ^{12}C, ^{16}O, ^{40}Ar, ^{81}Br, ^{107}Ag, and ^{138}Ba. The nine total extracted values of the imaginary diffuseness parameter a_I, for Region II of the potential, were then fit by an expansion in powers of $A^{\frac{1}{3}}$ as shown in Fig. 9 [9]. With this result, the current parameterization of the potential is given in Table II. An example using the potential is given in Fig. 10 for the integrated observables of ^{56}Fe and where "Modified potential" refers to Table II.

Lessons from the Construction and Use of the Two Potentials

Several conclusions (some of them tentative) come from the work summarized above. First, the medium-energy phenomenological optical potential is very forgiving, just like the low-energy phenomenological potential. In particular, several different projectile energy dependencies appear tractable (linear, logarithmic, exponential, ...) provided the total energy range is not excessive. Also, in a Schrödinger phenomenology, relatively small adjustments can be made in the parameters of the absorptive potential to improve agreement with the integrated observables without catastrophic consequences for the differential elastic and spin-dependent observables. In addition, it appears possible to obtain approximately smooth

Table II. Schrödinger global optical potential for nucleon–nucleus scattering in the target mass range $12 \leq A \leq 208$ and in the projectile energy range $50 \leq T \leq 400$ MeV.[3]

[2] For this reason the results have not been submitted for publication in a refereed journal.

[3] Strengths are in MeV and geometry is in fm; the upper (lower) signs refer to neutrons (protons); τ_3 is defined just below Eq. (3).

Real Central	$V_R = 105.5[1 - 0.1625ln(T)] \mp 16.5[(N-Z)/A] - (\frac{1}{2} + \tau_3)(0.4Z/A^{\frac{1}{3}})$ $r_R = 1.125 + T/10^3$, $T \leq 130$ $r_R = 1.255$, $T > 130$ $a_R = 0.675 + 3.1T/10^4$
Imag. Central	$W_V = 6.6 + 2.73(T-80)/10^2 + 3.87(T-80)^3/10^6$, $T \leq 140$ $W_V = 7.314 + 0.0462T$, $T > 140$ $r_I = 1.65 - 2.4T/10^3$, $T \leq 140$ $r_I = 1.17$, $T > 140$ $a_I = 0.27 + 2.5T/10^3$, $T \leq 140$ $a_I = 0.3537 + 0.08451A^{\frac{1}{3}} - 0.001835A^{\frac{2}{3}}$, $T > 140$
Real Spin-Orbit	$V_{SO} = 19.0[1 - 0.166ln(T)] \pm 3.75[(N-Z)/A]$ $r_{VSO} = 0.920 + 0.0305A^{\frac{1}{3}}$ $a_{VSO} = 0.768 - 0.0012T$, $T \leq 140$ $a_{VSO} = 0.60$, $T > 140$
Imag. Spin-Orbit	$W_{SO} = 7.5[1 - 0.248ln(T)]$ $r_{WSO} = 0.877 + 0.0360A^{\frac{1}{3}}$ $a_{WSO} = 0.62$

energy dependencies of the various observables with piecewise (continuous and discontinuous) parameterizations. [Note that this is not always the case for the transmission coefficients.] The Schrödinger phenomenology of Table II contains such parameterizations because the starting potential [7] was constructed in this way. In general, however, piecewise parameterization should clearly be avoided. Second, a Dirac phenomenology may provide physically realistic potentials over a wider projectile energy range than a Schrödinger phenomenology because the effective central potential in a second-order reduction involves squares and cross terms of the form factors appearing. This allows, for example, a "wine-bottle" shape. Third, in a Schrödinger phenomenology employing Woods-Saxon form factors, it appears that small adjustments in the imaginary diffuseness parameter a_I can fine tune the integrated observables with a minimal impact on the other observables. Perhaps the same is true in Dirac phenomenology? Fourth (and last), given the extreme sparseness of experimental medium-energy neutron scattering differential elastic and spin-dependent observables, a Dirac or relativistic Schrödinger phenomenological approach that is global in (1) projectile energy, (2) projectile isospin, and (3) target (Z,A), and uses the existing medium-energy proton and neutron (total cross sections) databases, appears to be a tractable way to calculate physically realistic neutron elastic scattering observables over wide ranges in energy and target. Whether a Dirac or relativistic Schrödinger formalism should be used has yet to be determined.

Current Work

Because a satisfactory global medium-energy nucleon-nucleus optical potential does not yet exist we are continuing our work on this goal. Currently, we are addressing an energy range of (perhaps) 20 MeV to (perhaps) 2000 MeV and a (spherical) target mass range of 16 to 209. The experimental database (currently over 20000 points) consists of the sets $\{d\sigma/d\Omega, \sigma_R, A_y, Q\}$ for protons and $\{\sigma_T$, some $d\sigma/d\Omega$ and $A_y\}$ for neutrons. Our approach is to consider both relativistic Schrödinger and Dirac phenomenology with the *identical* database in a nonlinear least-squares adjustment algorithm. Piecewise parameterizations will be inadmissable. We will also address a microscopic Dirac approach for the same ranges employing proton and neutron densities from recent work on the nuclear bound state problem using a relativistic Hartree approach [10]. Here, only even-even target nuclei will be considered. This topic is particularly exciting because the relativistic Hartree approach that we use is easily extended to relativistic Hartree-Fock [10] and, perhaps more importantly, we have discovered that our coupling constants are mostly *natural* (of order unity) when our Lagrangian is rewritten in a form that is based upon QCD scaling and chiral symmetry [11] and whose validity demands *naturalness*.

References

[1] R. Kozack and D. G. Madland, Phys. Rev. C **39**, 1461 (1989).

[2] A. M. Lane, Phys. Rev. Lett. **8**, 171 (1962); A. M. Lane, Nucl. Phys. **35**, 676 (1962).

[3] L. G. Arnold *et al.*, Phys. Rev. C **23**, 1949 (1981).

[4] R. S. Harding, Phys. Rev. **111**, 1164 (1958).

[5] R. Kozack and D. G. Madland, Nucl. Phys. **A509**, 664 (1990).

[6] R. Kozack and D. G. Madland, Nucl. Phys. **A552**, 469 (1993).

[7] P. Schwandt *et al.*, Phys. Rev. C **26**, 55 (1982).

[8] D. G. Madland, "Recent Results in the Development of a Global Medium-Energy Nucleon-Nucleus Optical-Model Potential," *Proceedings of a Specialists' Meeting on Preequilibrium Nuclear Reactions, Semmering, Austria, 1988*, edited by B. Strohmaier (OECD Nuclear Energy Agency, NEANDC-245'U', Paris, 1988) p. 103.

[9] I thank A. J. Sierk (private communication, June 1996) for performing this fit.

[10] B. A. Nikolaus, T. Hoch, and D. G. Madland, Phys. Rev. C **46**, 1757 (1992).

[11] J. L. Friar, D. G. Madland, and B. W. Lynn, Phys. Rev. C **53**, 3085 (1996).

Figure Captions

Fig. 1 χ^2/point/data set for p + ^{208}Pb scattering in the energy range 80–800 MeV for four energy dependencies.

Fig. 2 χ^2_{tot}/point for p + ^{208}Pb scattering in three energy ranges for three energy dependencies.

Fig. 3 Differential elastic cross sections for p + ^{208}Pb scattering at 200 MeV in the logarithmic and exponential models. The solid curves are obtained in calculations that use the Dirac global potential (Table I) which has been determined by simultaneously fitting neutron and proton data. The dashed curves are from calculations using a Dirac global potential in which only proton data have been fit.

Fig. 4 Spin observables for p + ^{208}Pb scattering at 200 MeV in the logarithmic and exponential models. The solid and dashed curves have the same explanation as in Fig. 3.

Fig. 5 Total cross sections for n + ^{208}Pb scattering from 95 to 250 MeV in the logarithmic and exponential models. The solid and dashed curves have the same explanation as in Fig. 3 and the dotted curve is the prediction of a geometric black disk model.

Fig. 6 Differential elastic cross sections and analyzing powers for n + ^{208}Pb scattering at 155 MeV in the logarithmic and exponential models. The solid and dashed curves have the same explanation as in Fig. 3. The calculations shown are *predictions* as the experimental data were not used in determining the potentials.

Fig. 7 Differential elastic cross sections and spin observables for nucleon-plus-^{208}Pb scattering at 100 MeV as predicted by the Dirac global logarithmic potential (Table I). The solid curves are the predictions for neutron scattering while the dashed curves are the predictions for proton scattering.

Fig. 8 Calculations of the proton total reaction cross section for the p + ^{27}Al reaction using the Schrödinger formalism, Eq. (19), in three different approaches with the identical optical potential.

Fig. 9 Empirical values of and polynomial fit to the imaginary diffuseness parameter a_I for Region II ($T_p > 140$ MeV) of the Schrödinger global potential of Table II.

Fig. 10 Comparisons of measured and calculated integral scattering observables from the nucleon-plus-^{56}Fe reaction using the Schrödinger formalism. The original potential is that of Schwandt *et al.* [7] and the modified potential is that of Table II.

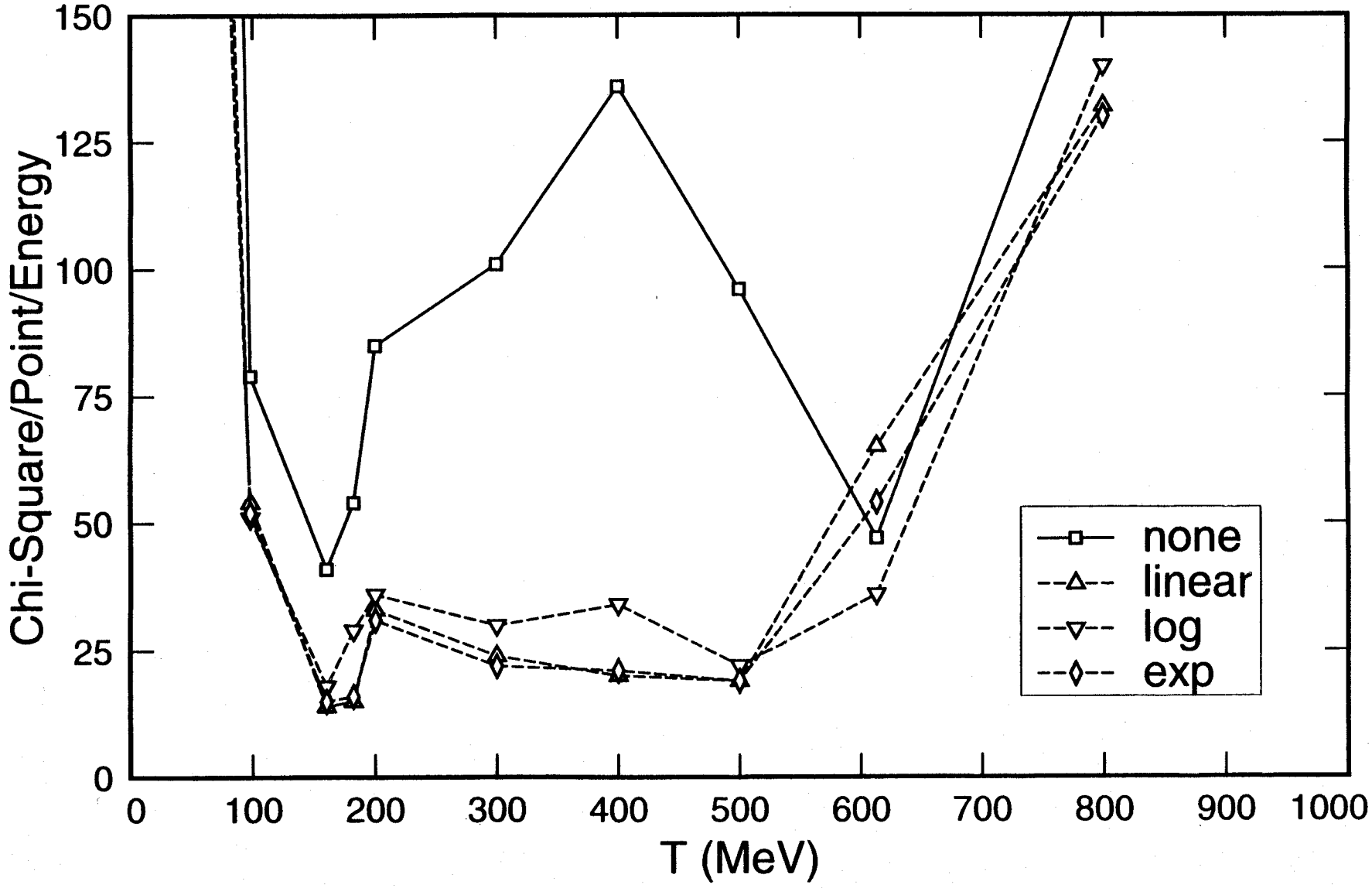
Chi-Square Values for p + 208-Pb Scattering
Four Energy Dependencies, 80 - 800 MeV
Chi-Square/Point/Energy
T (MeV)
0
25
50
75
100
125
150
0
100
200
300
400
500
600
700
800
900
1000
none
linear
log
exp

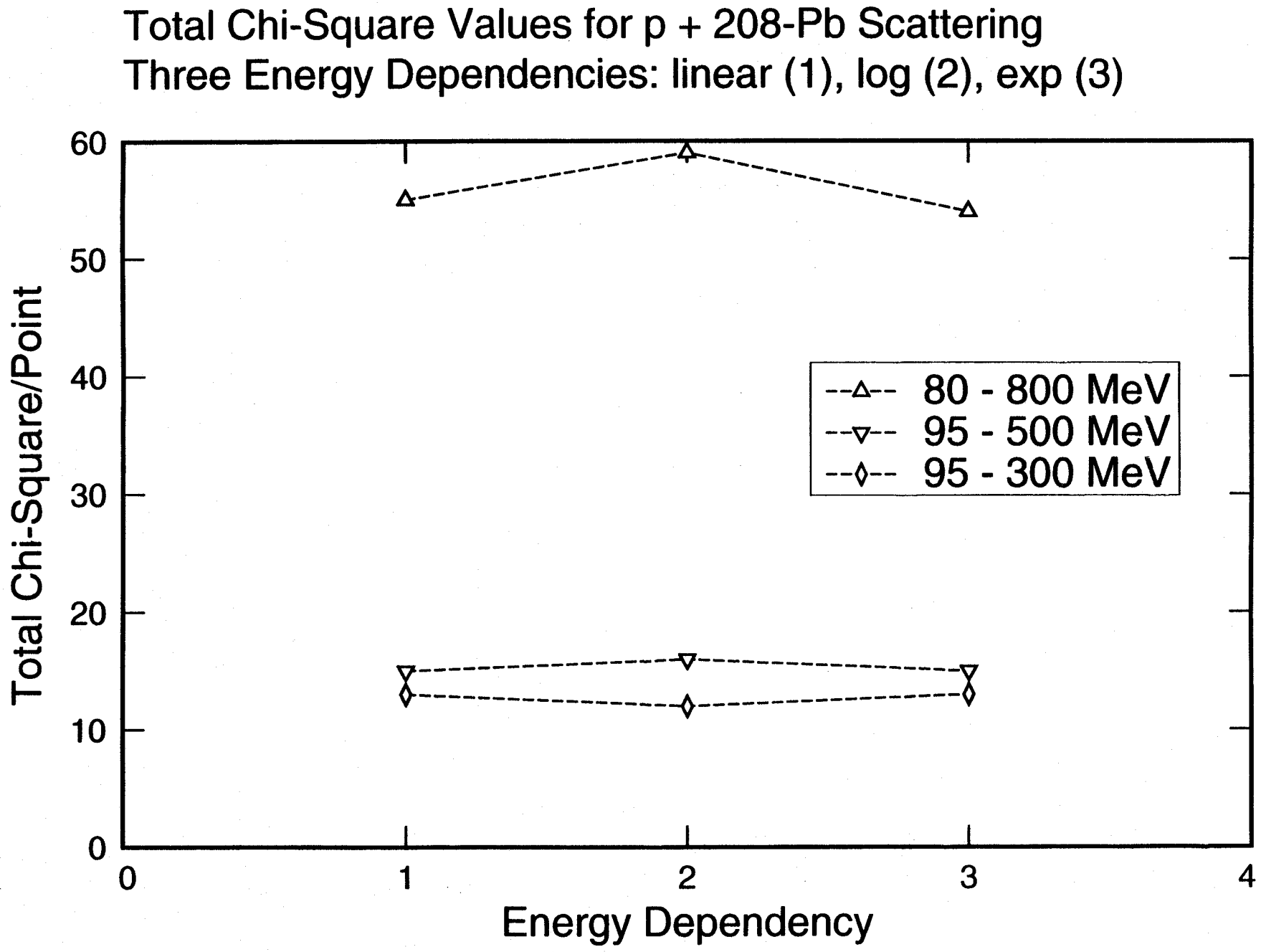
Total Chi-Square Values for p + 208-Pb Scattering
Three Energy Dependencies: linear (1), log (2), exp (3)
Total Chi-Square/Point
Energy Dependency
0
10
20
30
40
50
60
0
1
2
3
4
80 - 800 MeV
95 - 500 MeV
95 - 300 MeV

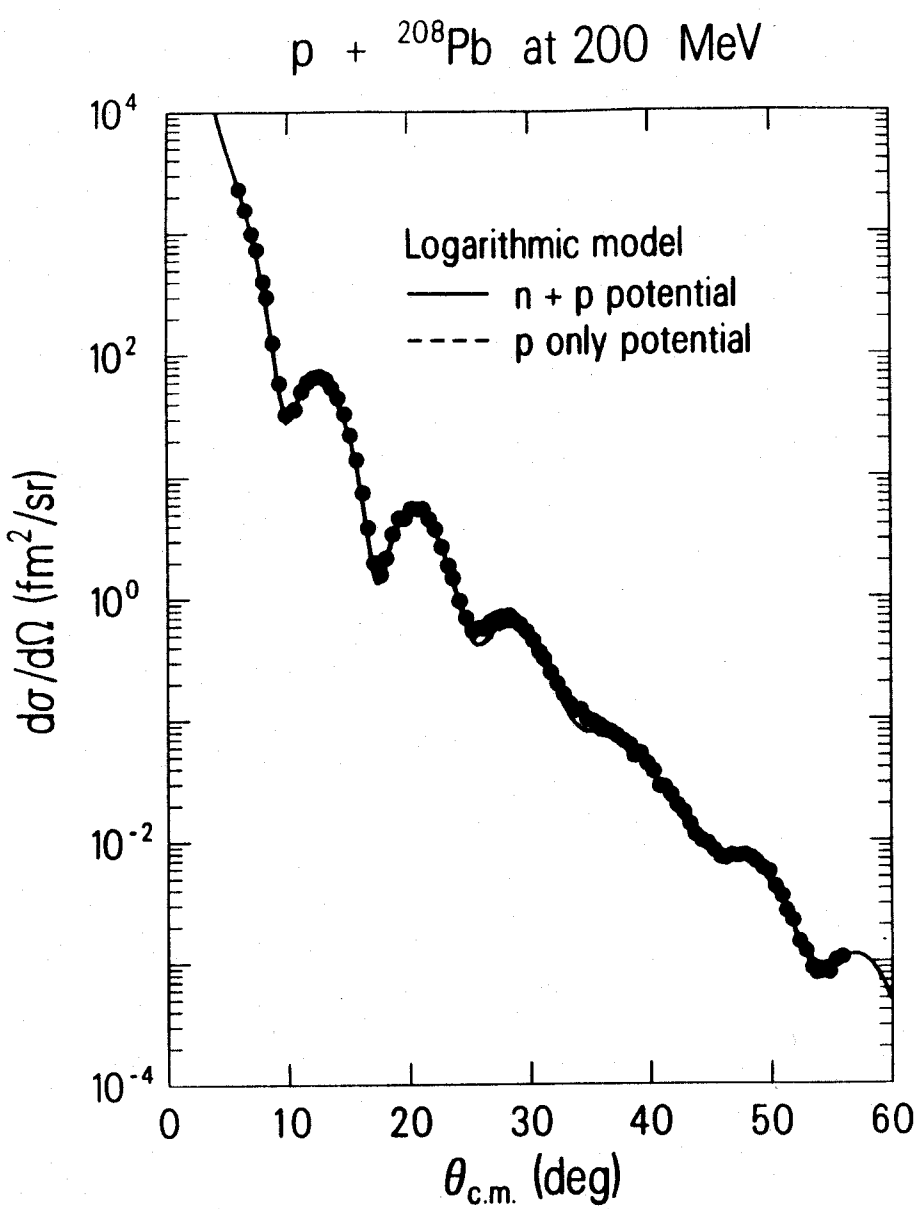
p + 208Pb at 200 MeV
Logarithmic model
n + p potential
p only potential
dσ/dΩ (fm²/sr)
θc.m. (deg)
10⁴
10²
10⁰
10⁻²
10⁻⁴
0
10
20
30
40
50
60

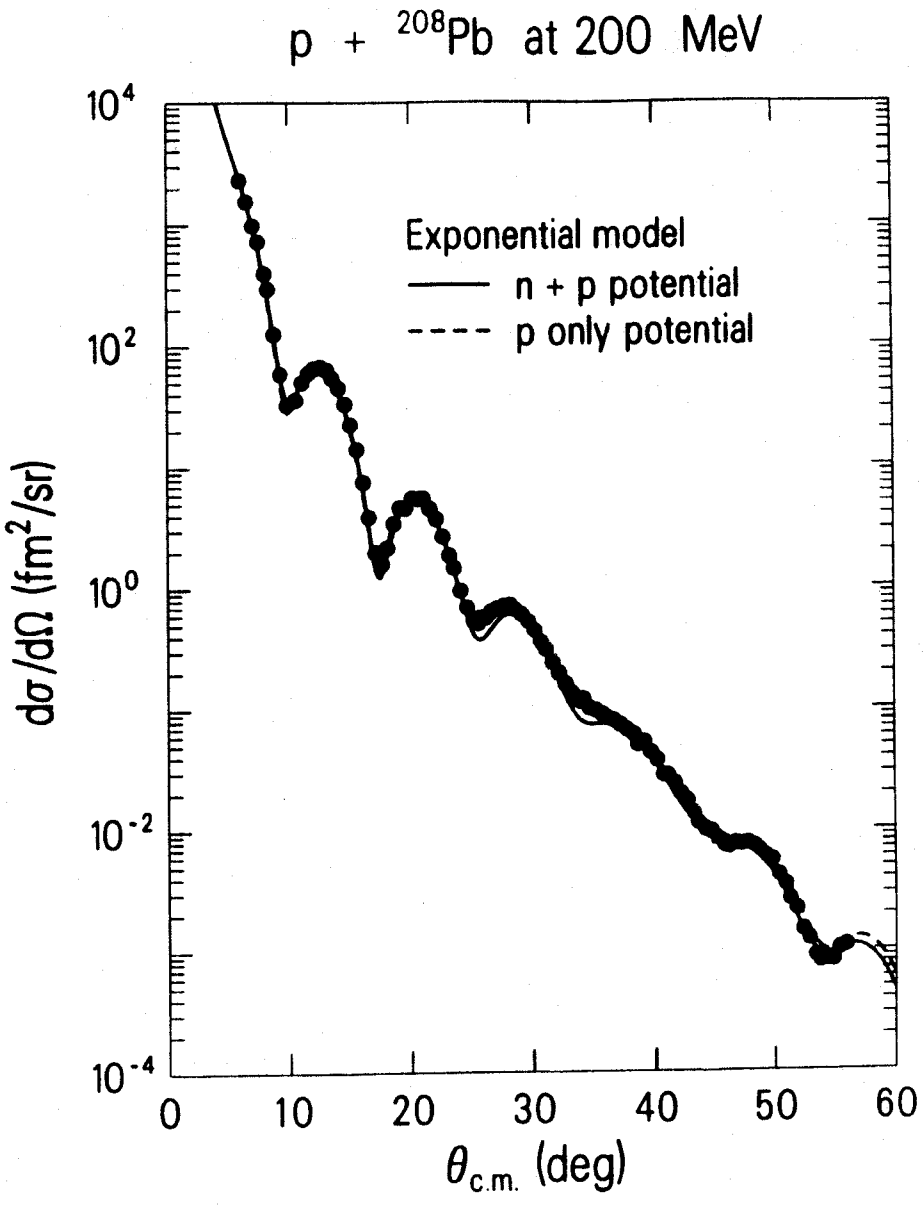
p + 208Pb at 200 MeV
Exponential model
n + p potential
p only potential
dσ/dΩ (fm²/sr)
θc.m. (deg)
10⁴
10²
10⁰
10⁻²
10⁻⁴
0
10
20
30
40
50
60

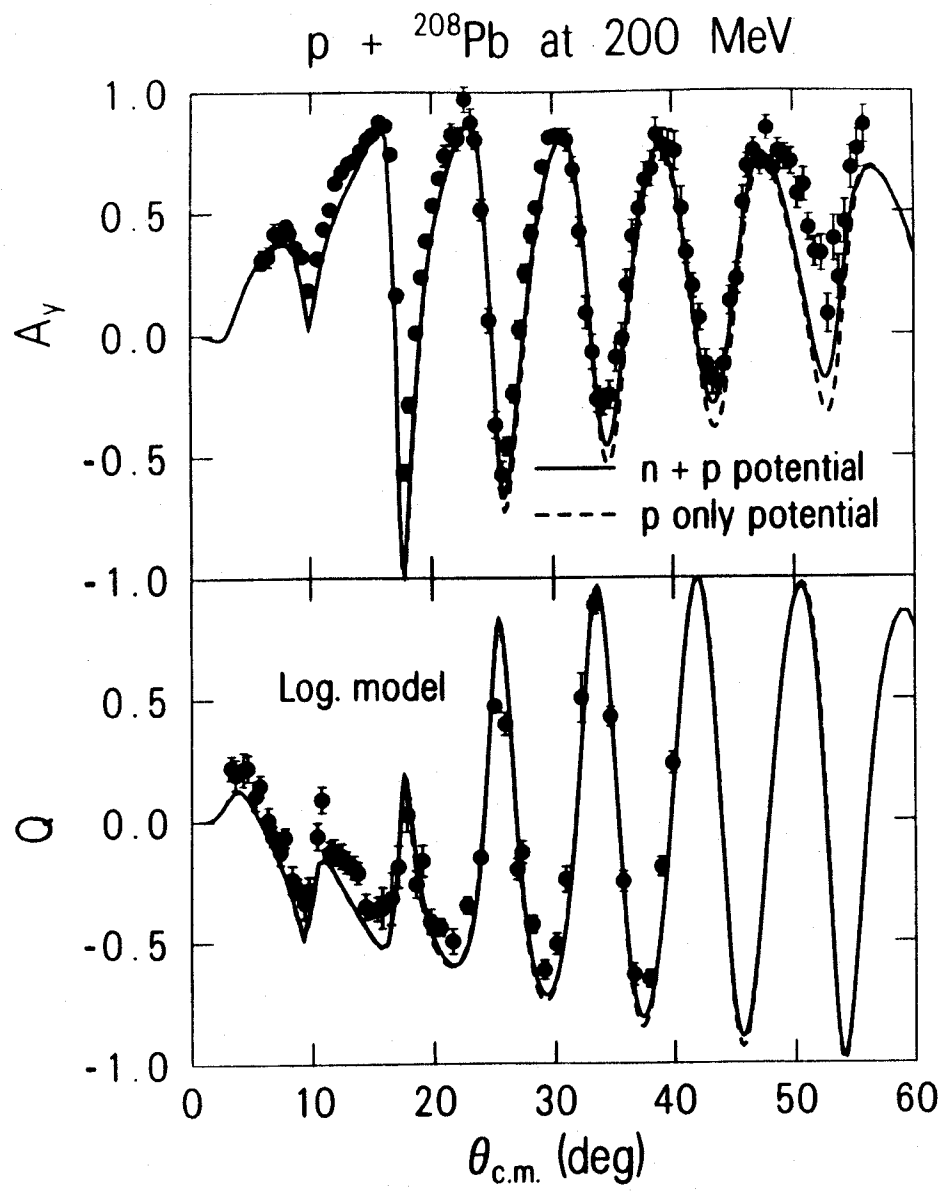
p + 208Pb at 200 MeV
Ay
1.0
0.5
0.0
-0.5
-1.0
n + p potential
p only potential
Log. model
Q
0.5
0.0
-0.5
-1.0
0
10
20
30
40
50
60
θc.m. (deg)

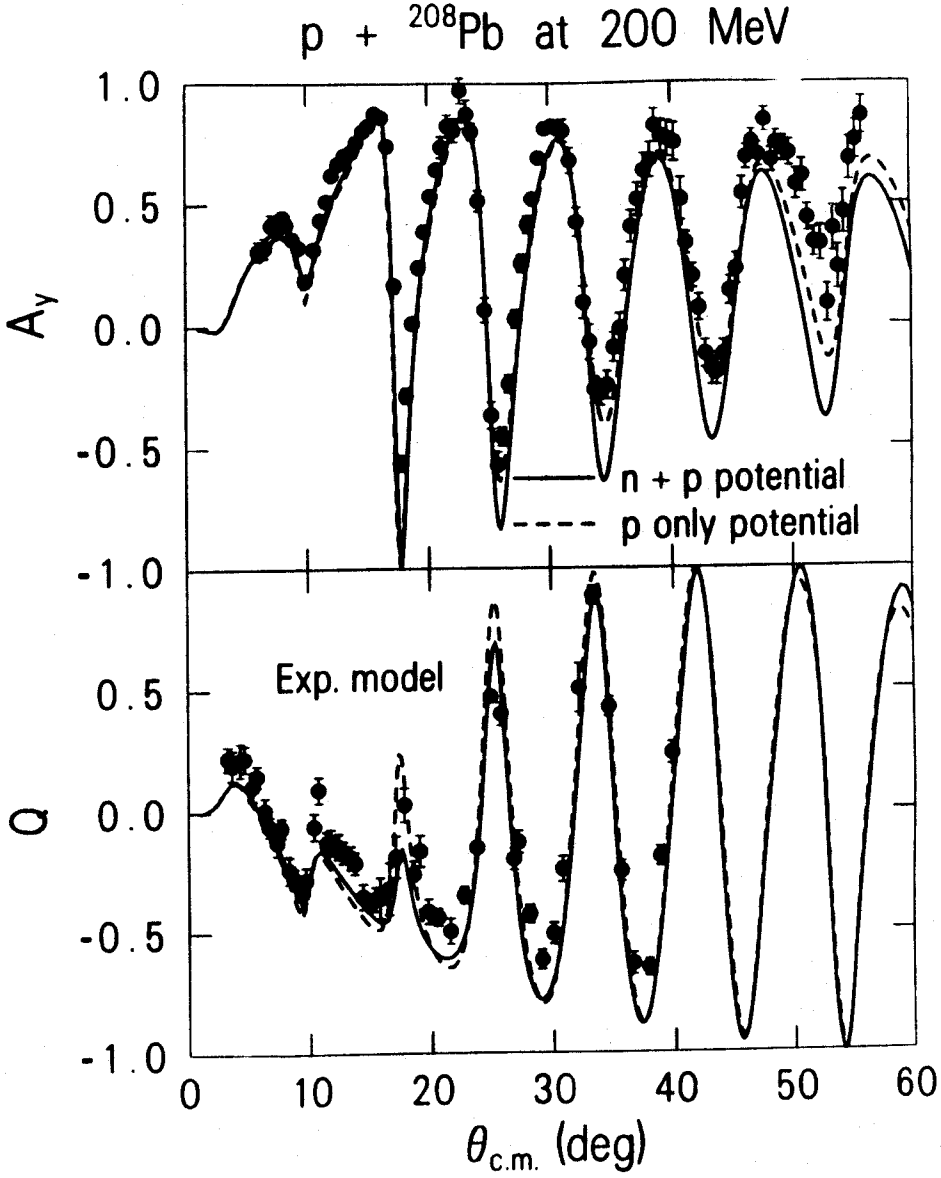
p + 208Pb at 200 MeV
Ay
1.0
0.5
0.0
-0.5
-1.0
n + p potential
p only potential
Exp. model
Q
0.5
0.0
-0.5
-1.0
0
10
20
30
40
50
60
θc.m. (deg)

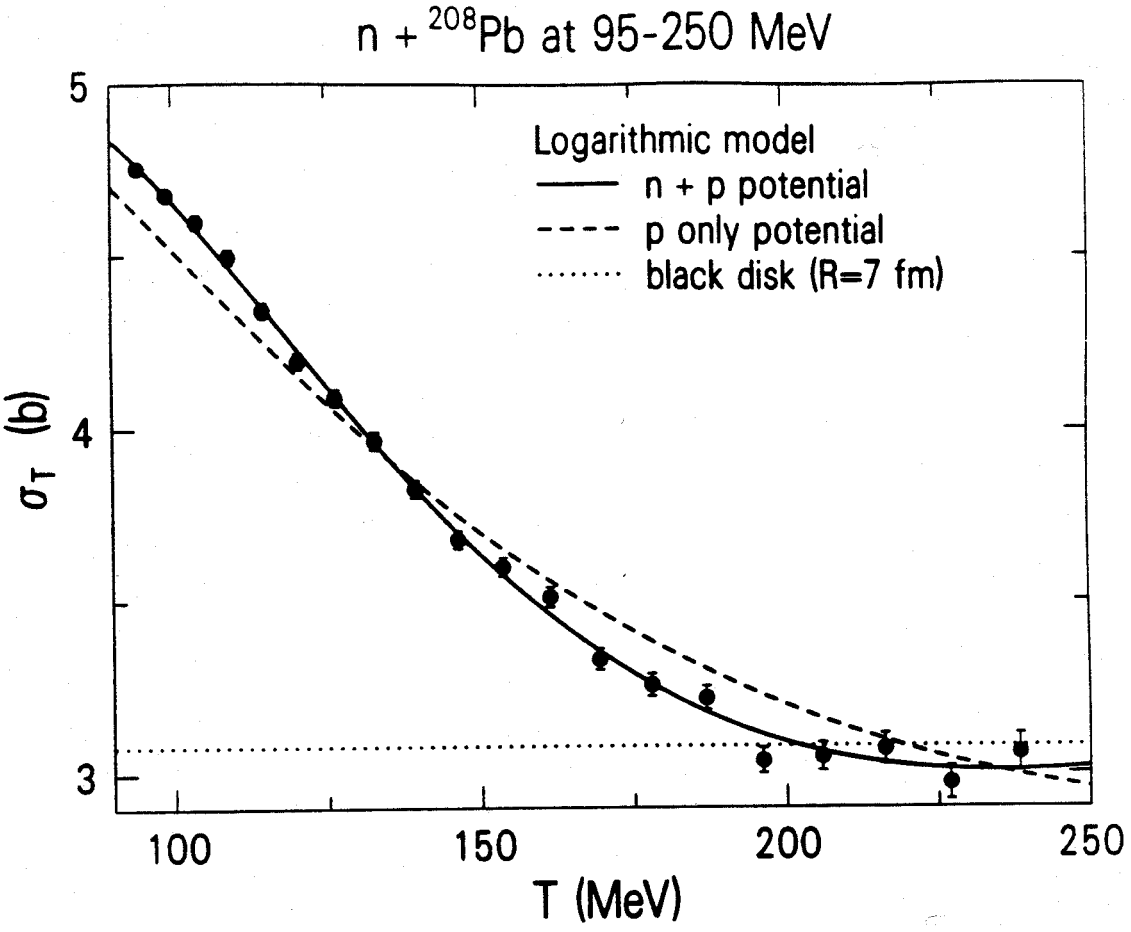
n + 208Pb at 95-250 MeV
Logarithmic model
n + p potential
p only potential
black disk (R=7 fm)
σT (b)
T (MeV)
5
4
3
100
150
200
250

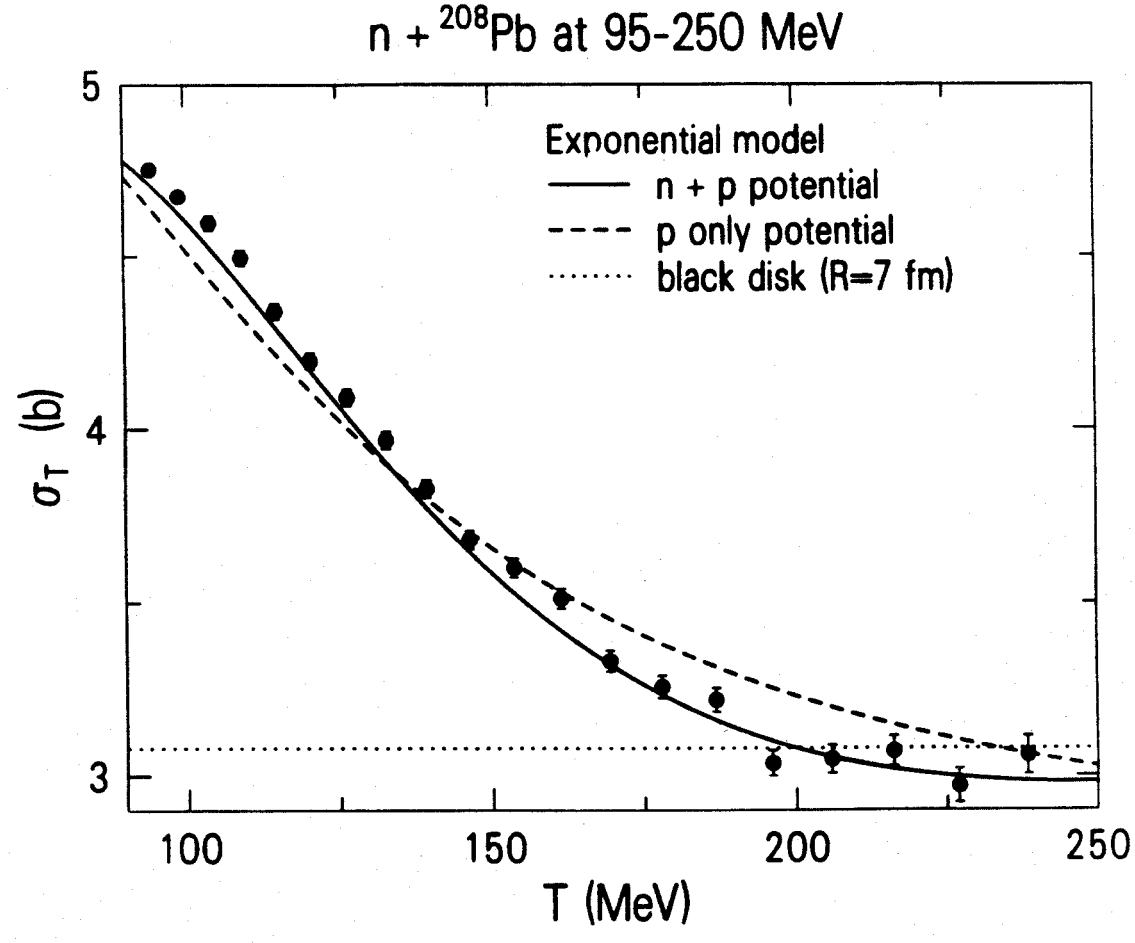
n + 208Pb at 95-250 MeV
Exponential model
n + p potential
p only potential
black disk (R=7 fm)
σT (b)
T (MeV)
5
4
3
100
150
200
250

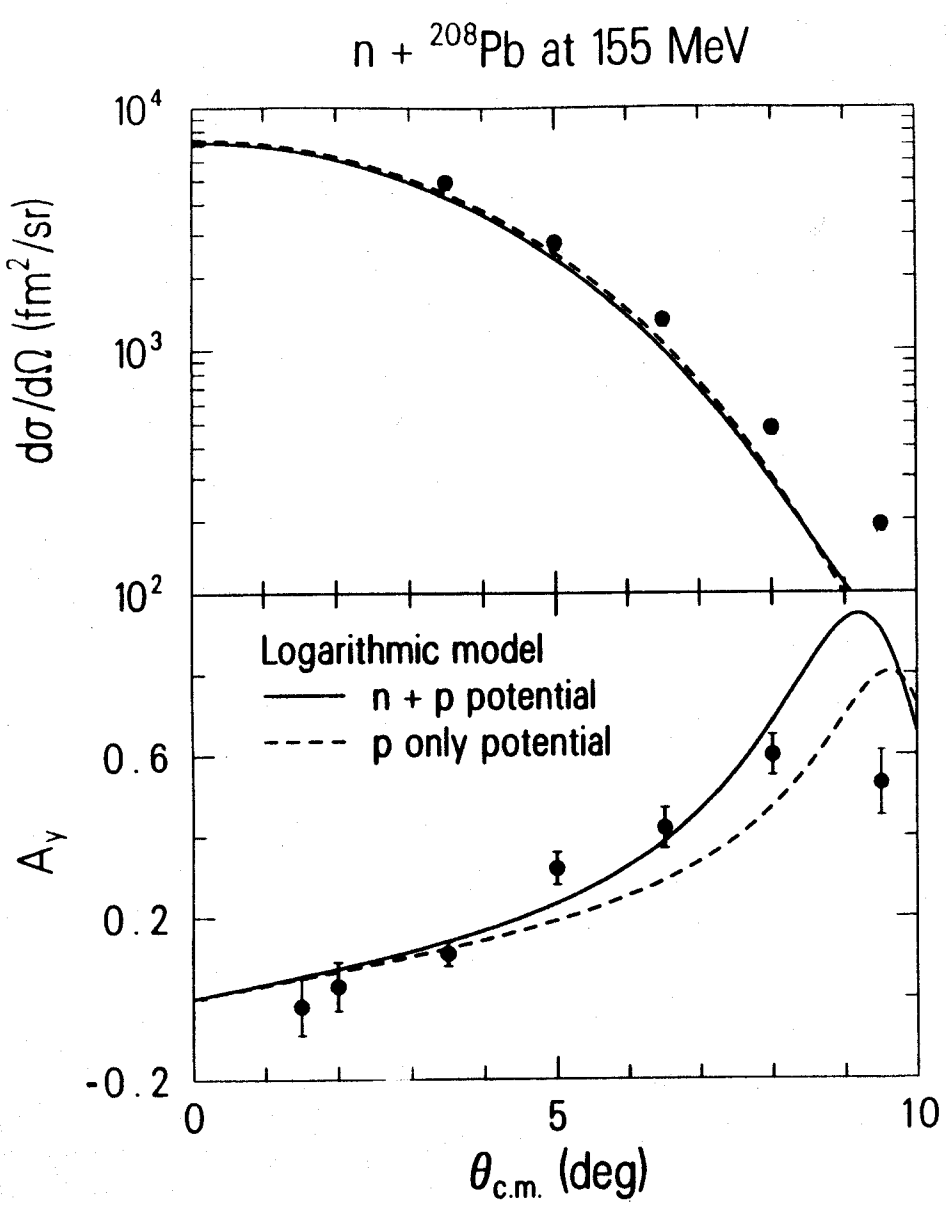
n + 208Pb at 155 MeV
dσ/dΩ (fm²/sr)
10⁴
10³
10²
Logarithmic model
n + p potential
p only potential
A_y
0.6
0.2
-0.2
0
5
10
θc.m. (deg)

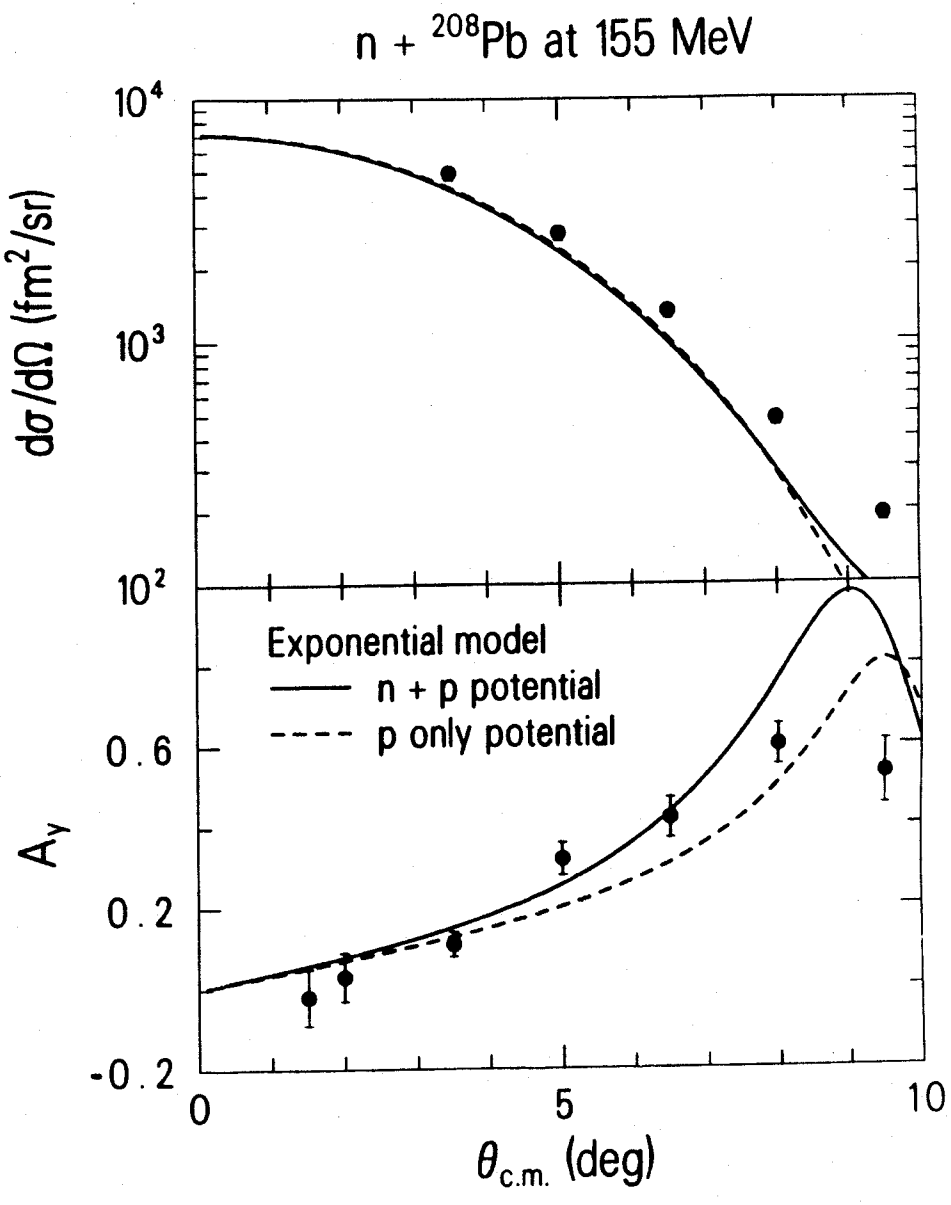
n + 208Pb at 155 MeV
dσ/dΩ (fm²/sr)
10⁴
10³
10²
Exponential model
n + p potential
p only potential
A_y
0.6
0.2
-0.2
0
5
10
θc.m. (deg)

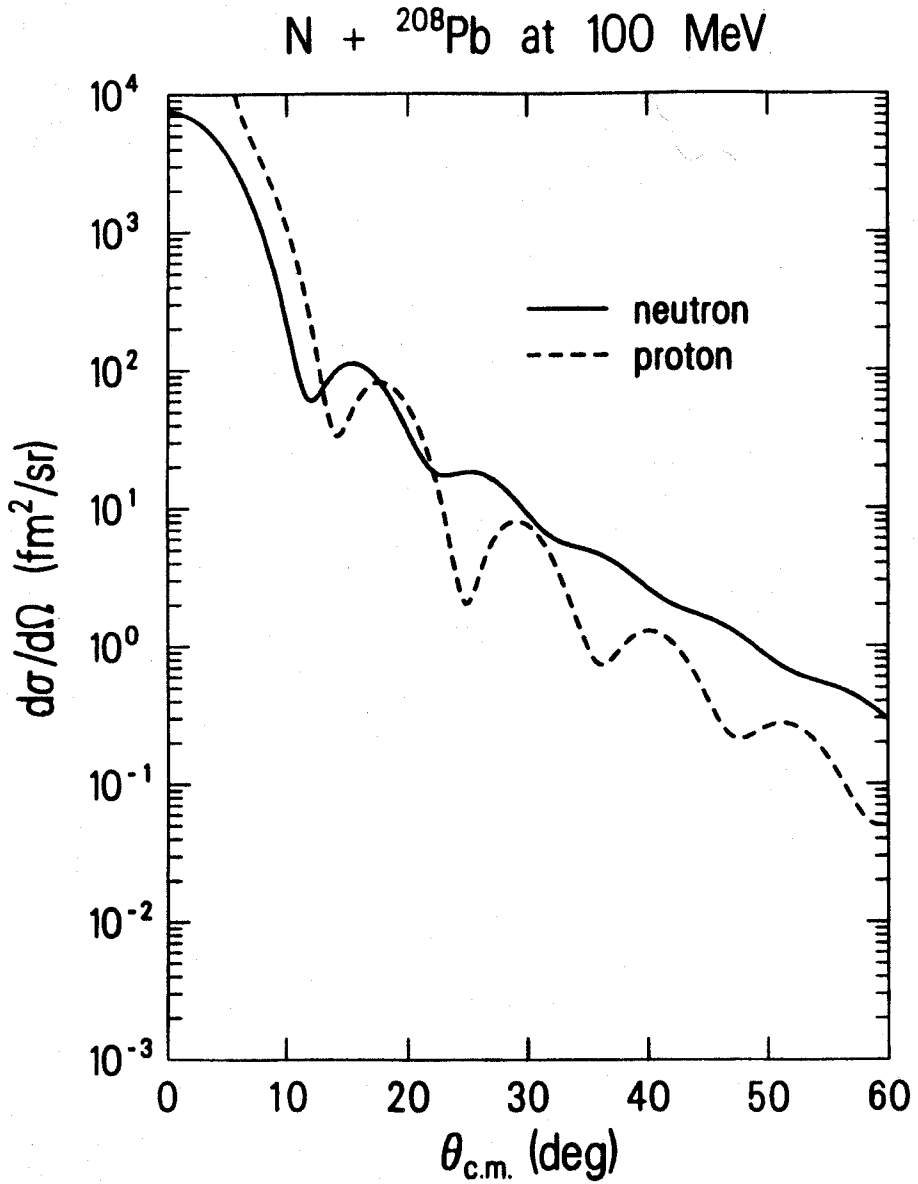
N + 208Pb at 100 MeV
dσ/dΩ (fm²/sr)
neutron
proton
θc.m. (deg)

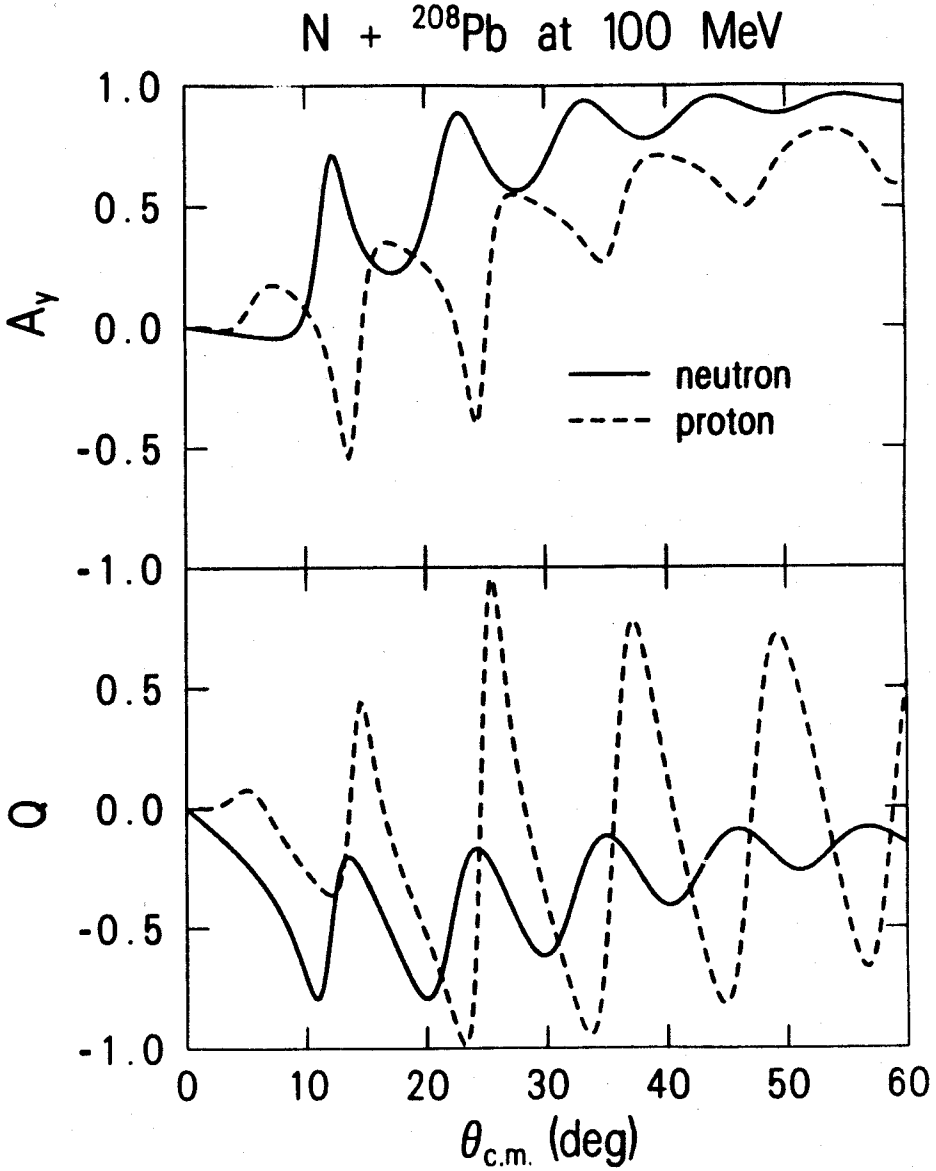
N + 208Pb at 100 MeV
Ay
Q
neutron
proton
θc.m. (deg)

p + 27-Al Total Reaction Cross Section
Schroedinger Formalism

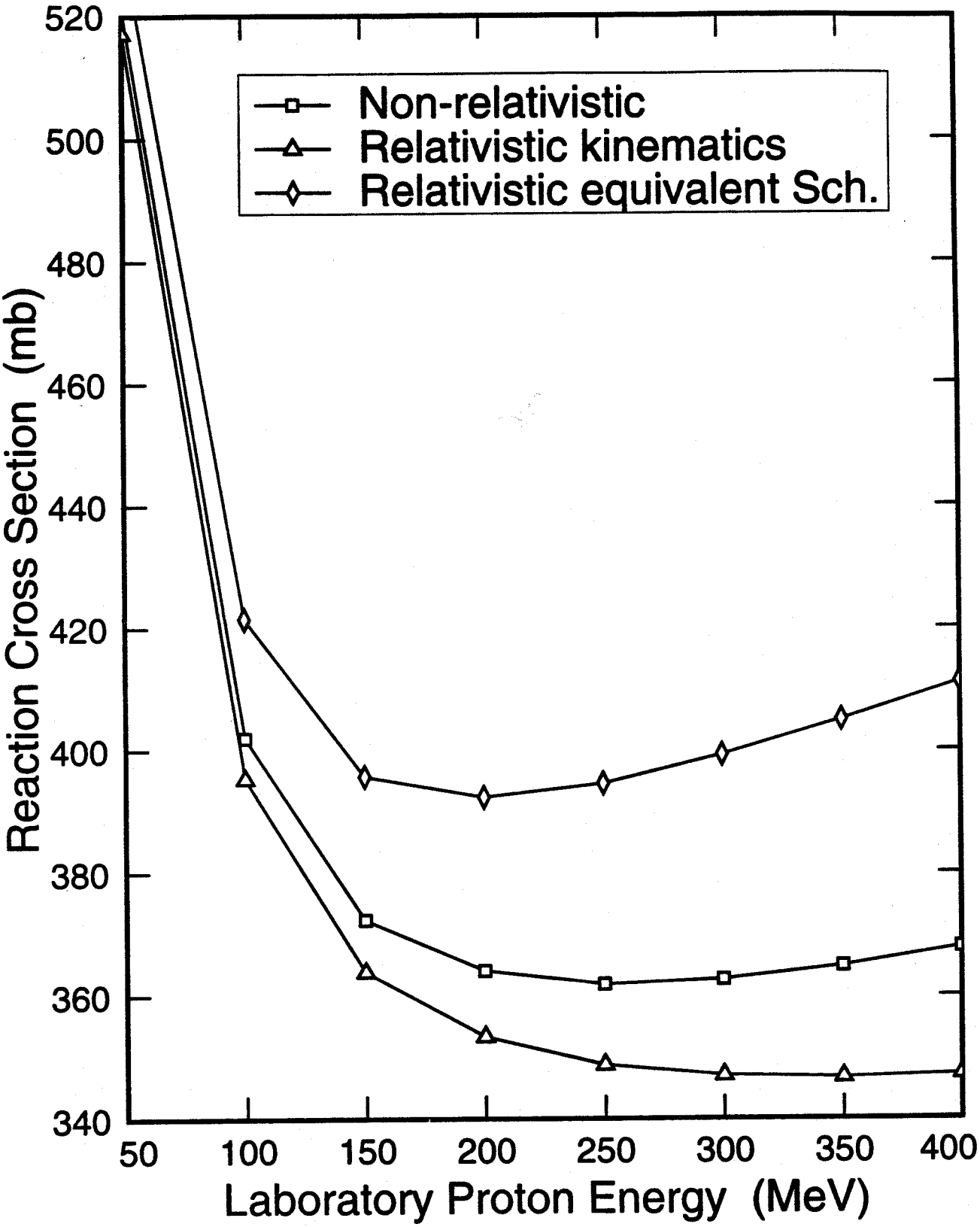

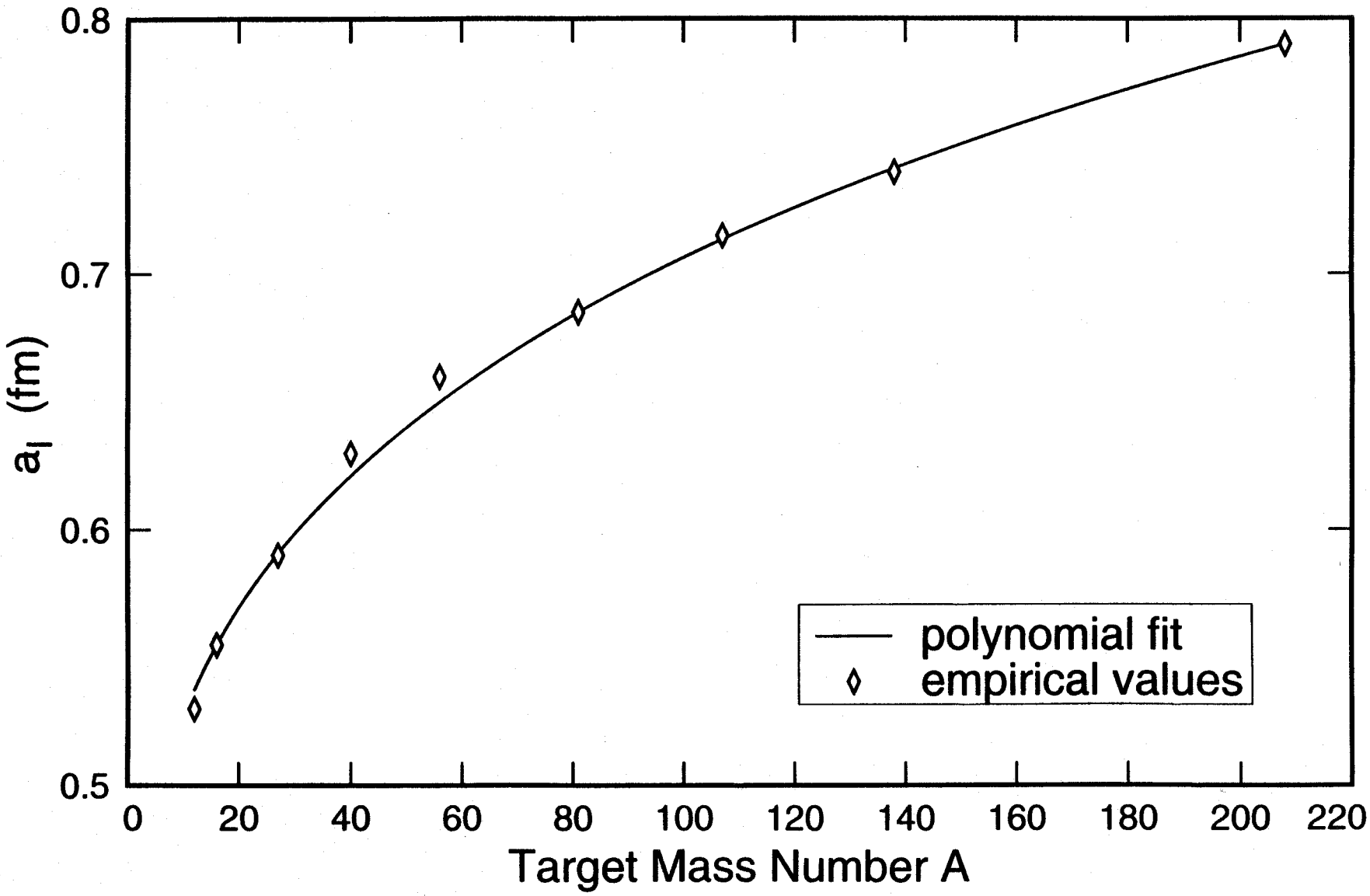
Improvement to Semmering Potential (Region II)
$a_l = 0.3537 + 0.08451A^{1/3} - 0.001835A^{2/3}$
0.8
0.7
0.6
0.5
a_l (fm)
0
20
40
60
80
100
120
140
160
180
200
220
Target Mass Number A
polynomial fit
empirical values

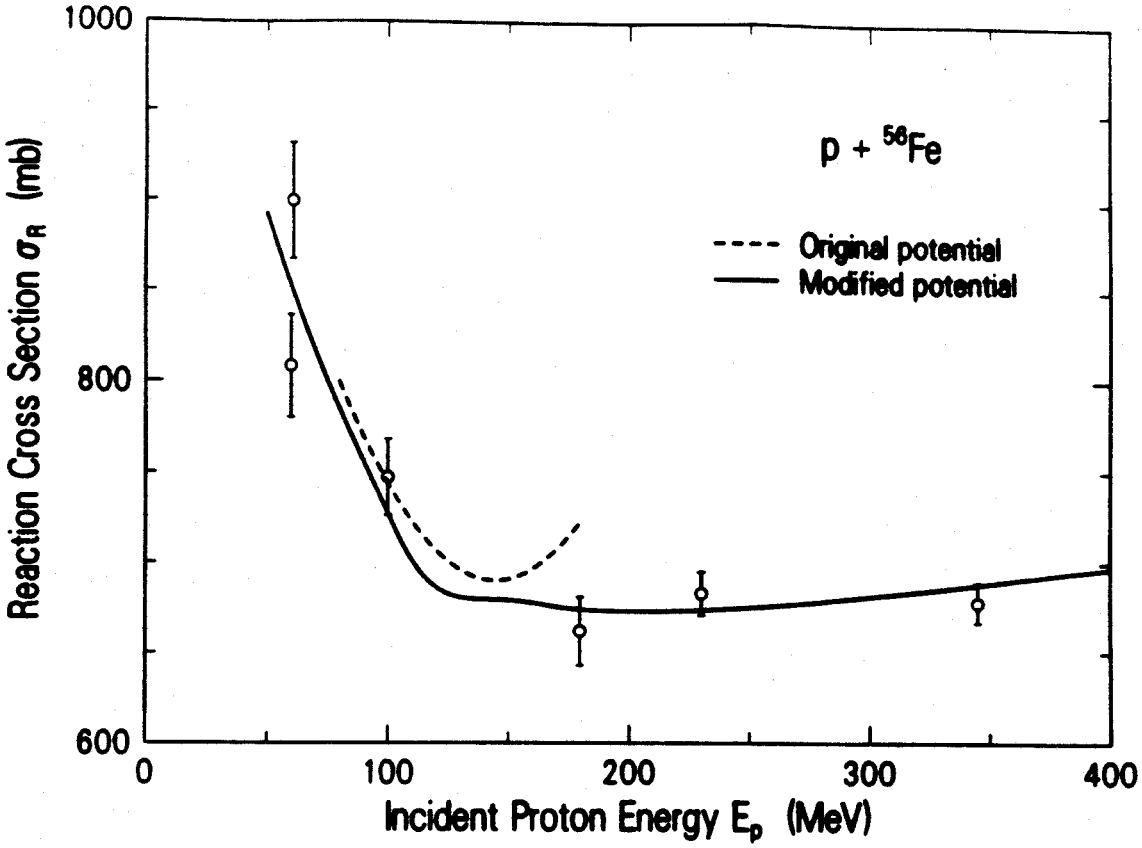
1000
800
600
0
100
200
300
400
Reaction Cross Section σ_R (mb)
Incident Proton Energy E_p (MeV)
p + ^{56}Fe
Original potential
Modified potential

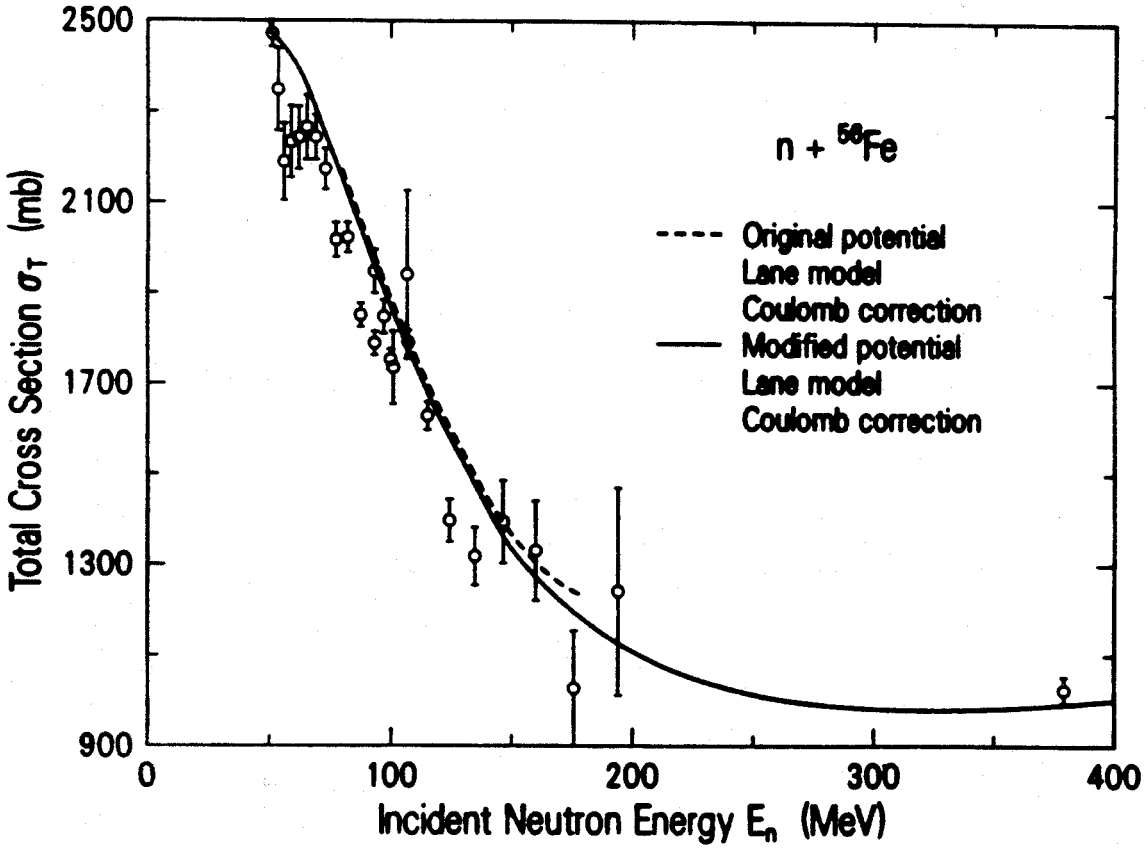
2500
2100
1700
1300
900
0
100
200
300
400
Total Cross Section σ_T (mb)
Incident Neutron Energy E_n (MeV)
n + ^{56}Fe
Original potential
Lane model
Coulomb correction
Modified potential
Lane model
Coulomb correction